Journal of Rare Earths 38 (2020) 175–181

Contents lists available at ScienceDirect

Journal of Rare Earths

journal homepage: http://www.journals.elsevier.com/journal-of-rare-earths

Ce–Fe–Mn ternary mixed-oxide catalysts for catalytic decomposition of ozone at ambient temperatures☆

Xiao Chen [a], Zhenglong Zhao [b], Shuo Liu [c], Jinxing Huang [c], Jing Xie [b], Ying Zhou [b], Zhiyan Pan [a, **], Hanfeng Lu [b, *]

[a] Institute of Environmental Chemicals and Resources, College of Environment, Zhejiang University of Technology, Hangzhou 310014, China
[b] Innovation Team of Air Pollution Control, Institute of Catalytic Reaction Engineering, College of Chemical Engineering, Zhejiang University of Technology, Hangzhou 310014, China
[c] Hangzhou Runxing Technology Co., Ltd., Hangzhou 310014, China

ARTICLE INFO

Article history:
Received 28 November 2018
Received in revised form
26 January 2019
Accepted 29 January 2019
Available online 25 July 2019

Keywords:
Rare earths modified
Ce–Fe–Mn mixed oxide
Oxygen vacancy
Ozone
Catalytic decomposition

ABSTRACT

Ce-modified Mn–Fe mixed-oxide catalysts were prepared by a citric acid sol-gel method and characterized by X-ray diffraction, Raman, N_2 adsorption-desorption, infrared spectra, H_2 temperature-programmed reduction and thermogravimetric analyses. Their catalytic properties were investigated in ozone (O_3) decomposition reaction. Results show that the small amount of rare earth metal Ce added during Mn–Fe (FM) mixed-oxide synthesis greatly improves the catalytic performance in O_3 decomposition. Among the prepared catalysts, the $C_{0.04}(FM)_{0.96}$ mixed-oxide catalyst exhibits the highest catalytic activity and stability. The O_3 conversion over $C_{0.04}(FM)_{0.96}$ is 98% after 24 h reaction at 25 °C under dry condition, and that over FM decreases to 90% after 16 h reaction. At 0 °C, the O_3 conversion over $C_{0.04}(FM)_{0.96}$ is 95% after 7 h reaction under dry condition, and that over FM slows down to 70%. Under humid condition (RH = 65%), the O_3 conversion over $C_{0.04}(FM)_{0.96}$ is 63% after 6.5 h reaction at 25 °C, while that over FM decreases to 55%. When Ce is doped into Mn–Fe mixed oxides, the small amount of Ce enters the crystal lattice of MnO_2, and partial Fe is separated to form Fe_2O_3. This changes cause lattice distortion and increase defects and enable the as-synthesized Ce–Fe–Mn ternary mixed-oxide catalysts to acquire additional oxygen vacancies and increase their specific surface area, thereby increasing the number of reaction sites and enhancing the catalytic performance of the catalysts forO_3 decomposition.

© 2020 Published by Elsevier B.V. on behalf of Chinese Society of Rare Earths.

1. Introduction

Ozone (O_3) layer is like a protective umbrella that protects people, animals, and plants on earth from ultraviolet light and O_3 plays an important role in food preservation, health care, and environment treatment because of its strong oxidizing ability.[1–6] However, tropospheric O_3 is a common pollutant that causes health problems to human beings.[7] In fact, O_3 concentrations exceeding 1×10^{-7} (volume ratio) cause distress to humans and extremely high O_3 concentrations are fatal. The World Health Organization stipulates that O_3 concentration in air should be lower than 1×10^{-7}.[8] The rapid development of various industries led to significant increases in nitrogen oxide (NO_x) and volatile organic compound (VOC) emissions. The photochemical reactions of NO_x and VOCs in turn increases O_3 concentrations in the air.[9–11] When O_3 is used in sterilization and disinfection or pollutant degradation, residual O_3 in stream usually exceeds the allowable concentration. Moreover, some office and household appliances, such as duplicator, printer, and ozone disinfector also emit a certain amount of O_3.[12] Therefore, eliminating O_3 in the air is an urgent task, which requires a safe and effective ozone removal method.[13]

Various methods for removing O_3,[14–16] such as thermal decomposition, activated carbon adsorption, liquid absorption, and catalytic decomposition are currently available. Among them, catalytic decomposition technique has been generally adopted for O_3 removal due to its safety, economy, and high efficiency. In particular, manganese oxide (MnO_x)-based catalysts are extensively studied because of their low cost and because they are

☆ **Foundation item**: Project supported by the National Natural Science Foundation of China (21506194, 21676255), the Natural Science Foundation of Zhejiang Province (Y16B070011), the Commission of Science and Technology of Zhejiang province (2017C03007, 2017C33106).
* Corresponding author.
** Corresponding author.
E-mail addresses: panzhiyan@zjut.edu.cn (Z.Y. Pan), luhf@zjut.edu.cn (H.F. Lu).

https://doi.org/10.1016/j.jre.2019.01.010
1002-0721/© 2020 Published by Elsevier B.V. on behalf of Chinese Society of Rare Earths.

environment-friendly, have excellent tunable structural, and promote O_3 catalytic decomposition at room temperature.[17–19] Jia et al. synthesized three kinds of manganese dioxide with different crystal structures (α-, β- and γ-MnO_2) by hydrothermal method and found that α-MnO_2 had the highest catalytic activity of O_3 decomposition.[20] They also synthesized Fe-MnO_x (Mn/Fe molar ratio = 2) with increased oxygen vacancies and enhanced activity by adding Fe during α-MnO_2 synthesis.[21] Lian et al. studied the influence of different iron precursors and Mn/Fe ratios on the catalytic O_3 decomposition activity and found that the catalytic performance over $MnFe_{0.5}O_x$-$Fe(NO_3)_3$ was the best.[22] Liu et al. found that, compared with pure todorokite MnO_2 catalyst, Ce-modified todorokite MnO_2 samples exhibited considerably better activity and stability for O_3 decomposition.[23] Many reports showed that the oxygen vacancy is the active site for O_3 decomposition. The content of oxygen vacancies is a decisive factor in catalytic O_3 decomposition.[20–24] Based on this mechanism, we believe that the introduction of more oxygen vacancies in the materials can further improve their catalytic properties in O_3 decomposition.

Adding a third element to a binary mixed oxide can change the number of oxygen vacancies and alter crystal phase structures and improving oxygen storage capacities and stability of mixed oxides.[25–27] However, to the best of our knowledge, the ternary mixed-oxides applied in the catalytic decomposition of O_3 is rarely reported despite their great significance to scientific research and practical application owing to their excellent performance and special and variable structures.[28] Herein, based on the Mn–Fe (Mn/Fe molar ratio = 2) binary mixed-oxide catalyst reported in the literature, we prepared the Ce–Mn–Fe ternary mixed-oxide catalysts by citric acid sol-gel method, and the effects of rare earth metal Ce modification on the catalyst structure and catalytic O_3 decomposition performance are also clarified.

2. Experimental

2.1. Chemical agents

Manganese nitrate ($Mn(NO_3)_2$, 50 wt%) was purchased from Shanghai Macklin Biochemical Co., Ltd. Iron nitrate ($Fe(NO_3)_3{\cdot}9H_2O$) was purchased from Shanghai Lingfeng Chemical Reagent Co., Ltd. Cerium nitrate ($Ce(NO_3)_3{\cdot}6H_2O$) was purchased from Sinopharm Chemical Reagent Co., Ltd., and citric acid ($C_6H_8O_7{\cdot}H_2O$) was purchased from Rugao Jinling Reagent Co.

2.2. Catalyst preparation

Ce–Fe–Mn mixed-oxide catalysts were prepared by citric acid sol-gel method with appropriate amounts of Mn, Fe and Ce nitrates as precursors. $Mn(NO_3)_2$, $Fe(NO_3)_3{\cdot}9H_2O$ and $Ce(NO_3)_3{\cdot}6H_2O$ were mixed in appropriate molar ratios (the molar ratio of Mn/Fe is 2:1) in distilled water to obtain a transparent solution. Then citric acid equimolar to the metal nitrates was added to the solution. The mixed solution was stirred to form a sol in a water bath at 90 °C and then dried at 110 °C to form a fluffy gel. This gel was then calcined at 400 °C for 3 h in air. The synthesized catalysts were denoted as $C_x(FM)_{1-x}$, where $x/(1-x)$ represents the molar ratios of Ce/(Mn–Fe) (x = 0, 0.02, 0.04, 0.06). The purchased ozone decomposition catalyst was denoted as COC (main composition (detected by XRF): w(C) 95.06%, w(Mn) 1.39%, w(Fe) 0.820%, w(Si) 0.782%, w(Na) 0.394%, w(Al) 0.368%, w(Mg) 0.214%, w(S) 0.134%).

2.3. Catalyst characterization

X-ray diffraction (XRD) patterns were recorded on a PANalytical X′ Pert PRO diffractometer instrument operated at 40 kV and 30 mA with Cu Kα ray radiation (λ = 0.154178 nm). Scans were taken with a 2θ range from 10° to 80°.

The Raman spectra were measured on a microscopic confocal Raman spectrometer (HORIBA HR800) in the range of 200–1200 cm^{-1} three times, and the excitation source used had a wavelength of 532 nm.

N_2 adsorption-desorption isotherms of the samples were carried out at 77 °C on a Micromeritics ASAP2020 instrument. The specific surface areas and the mesopore sizes of the samples were calculated by using the Brunauer-Emmett-Teller (BET) and Barrett-Joyner-Halenda method, respectively. The samples were pretreated in vacuum at 200 °C for 5 h before measurements.

Infrared spectra were examined through Fourier transform infrared (FTIR) spectroscopy (Vertex 70, Bruker Optics, Germany). The samples were blended with KBr and pressed into tablets before measurement. Spectra were recorded from 400 to 4000 cm^{-1} at a resolution of 2.5 cm^{-1} and at an average of 32 scan/s.

H_2 temperature-programmed reduction (H_2-TPR) was measured on a FINE SORB-3010 E instrument equipped with a thermal conductivity detector (TCD). The sample was placed in a quartz reactor, pretreated in Ar flow at 200 °C for 1 h and cooled down at 50 °C. The catalyst bed was performed by admitting a flow of 5 vol% H_2/Ar at 60 °C for 10 min, followed by heating at a constant rate (10 °C/min) of up to 800 °C. Finally, the catalyst was cooled under Ar flow. The flow rates in the experiment were 30 mL/min. The hydrogen consumption was monitored using the TCD operating at 60 °C and 60 mA.

Thermogravimetric (TG) analysis was conducted on a Netzsch STA 409 PC. The samples were loaded into a pan, and the temperature was increased to 900 °C at a heating rate of 10 °C/min in O_2 or N_2 stream (50 mL/min).

2.4. Catalytic activity test

Catalytic decomposition ozone was carried out with a fixed-bed flow reactor (i.d. 6 mm). A total of 50 mg of catalyst mixed with 200 mg of quartz sand was packed in a reactor and then placed in a water bath at 25 °C (or 0 °C). The total flow rate, containing 21 ppm O_3 with different relative humidities, through the reactor was maintained at 400 mL/min; and the weight space velocity was set at 480000 mL/(g·h). The O_3 was generated by passing the dry oxygen through an O_3 generator (ZA-D 3G, Guangzhou Zeao Ozone equipment Co., Ltd., China). The inlet and outlet O_3 were analyzed by using an online FTIR spectrophotometer (Vertex 70, Bruker Optics, Germany), and the O_3 concentration was calculated by using the standard curve. The O_3 conversion was obtained on the basis of the inlet and outlet O_3 concentrations.

3. Results and discussion

3.1. Crystal structure and textural properties

The XRD patterns of the samples before and after Ce doping are shown in Fig. 1(a). The main crystal phase of the $C_x(FM)_{1-x}$ mixed oxides was ramsdellite MnO_2. In the case of six-coordinated, the ionic radii of Fe^{3+} (0.055 nm) and Mn^{4+} (0.053 nm) are similar; hence, substitution of Mn^{4+} by Fe^{3+} is easier, and the latter can be uniformly distributed in MnO_2, which leads to the lack of characteristic peaks of iron species in the FM sample. Given that the ionic radius of Ce^{3+} (0.102 nm) is larger than that of Mn^{4+}, a small amount of Ce enters into the MnO_2 lattice, which causes lattice distortion and replacement of some Fe^{3+}. This resulted in the change in the crystal growth direction and precipitation of some Fe_2O_3[29]; hence, the diffraction peaks of MnO_2 (101) crystal plane and Fe_2O_3 were detected. Compared with FM sample, the diffraction peaks of MnO_2 were obviously weakened after Ce doping,

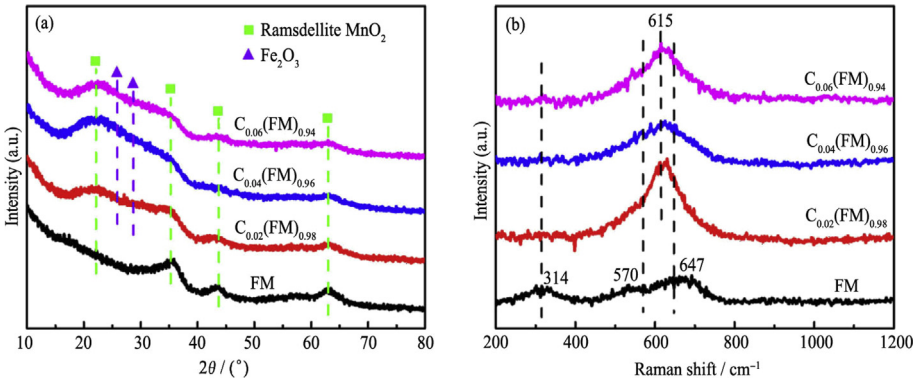

Fig. 1. XRD patterns (a) and Raman spectra (b) of $C_x(FM)_{1-x}$ mixed-oxide catalysts.

indicating that the defects (such as oxygen defects) of mixed oxides were increased, which is more beneficial to oxygen movement.[23]

The Raman spectra of $C_x(FM)_{1-x}$ mixed oxides are displayed in Fig. 1(b). The FM sample exhibited three bands at 316, 570 and 647 cm^{-1}, which are characteristic of the deformation modes of Mn–O–Mn and the stretching mode of the Mn–O lattice.[30] However, the Raman intensity of MnO_2 was weakened relative to that of the FM sample after Ce doping, and the Raman band of Fe_2O_3 (615 cm^{-1}) appeared.[31] These results are consistent with those of XRD characterization.

The texture structures of the $C_x(FM)_{1-x}$ mixed oxides were evaluated through N_2 adsorption-desorption technique. Table 1 lists some data about textural parameters of the samples derived from N_2 adsorption-desorption. The FM sample exhibited the smallest specific surface area (S_{BET}) and the largest average radius. After Ce doping, the S_{BET} increased, and the average radius decreased. Particularly, the S_{BET} increased as the Ce increased from 0 to 0.04 (molar ratio) but decreased as the Ce further increased to 0.06. This phenomenon can be understood as follows. First, the defects brought by Ce modification will result in increase in S_{BET}.[23] Second, the formed Fe_2O_3 after Ce doping will partially block the pores thereby resulting in decrease in S_{BET}. Thus, the S_{BET} increases at first then decreases as the Ce content increased from 0 to 0.06. Among the mixed oxides, $C_{0.04}(FM)_{0.96}$ had the largest specific surface area, which is suitable for heterogeneous catalytic oxidation reactions.[32]

Table 1
Texture structure of $C_x(FM)_{1-x}$ mixed oxide catalysts.

Sample	Average radius (nm)	Pore volume (cm^3/g)	S_{BET} (m^2/g)
FM	4.65	0.219	103
$C_{0.02}(FM)_{0.98}$	4.11	0.244	128
$C_{0.04}(FM)_{0.96}$	3.86	0.283	146
$C_{0.06}(FM)_{0.94}$	3.63	0.222	131

The surface functional groups of $C_x(FM)_{1-x}$ mixed oxides were measured by FT-IR. The results are shown in Fig. 2. The IR bands located at below 1000 cm^{-1} correspond to the M (Mn, Fe and Ce)–O stretching vibrational mode.[33–35] The IR band at around 1500 cm^{-1} can be assigned to the vibrational mode of the oxygen functional groups.[36] The intensity of this band decreased after Ce doping, which may be caused by oxygen defects. In addition, a weak peak was observed at 2350 cm^{-1}, which corresponds to the physically adsorbed CO_2. The intensity of this peak increased after Ce doping. This is because the addition of Ce introduces more oxygen vacancies, which enhance the ability of mixed-oxide to absorb CO_2.[37] These results indicate that Ce-containing samples have more oxygen vacancies, which is beneficial for O_3 decomposition.

3.2. Temperature-programmed studies

The effect of Ce addition on the amount of oxygen vacancies was further investigated by H_2-TPR. Fig. 3 shows the H_2-TPR profiles of

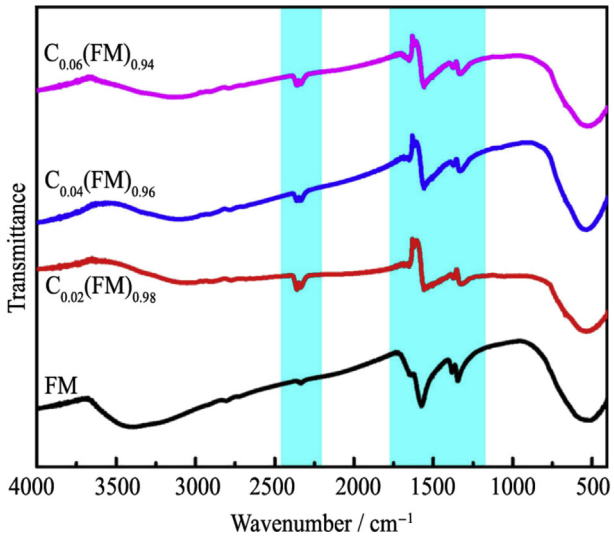

Fig. 2. FTIR spectra of $C_x(FM)_{1-x}$ mixed oxide catalysts.

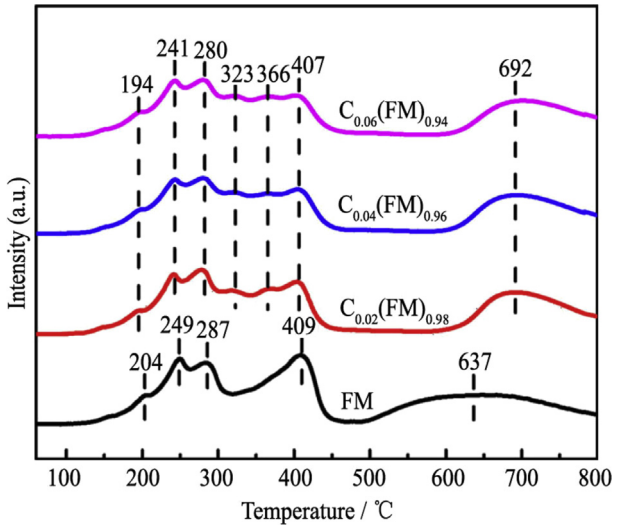

Fig. 3. H_2-TPR profiles of $C_x(FM)_{1-x}$ mixed oxide catalysts.

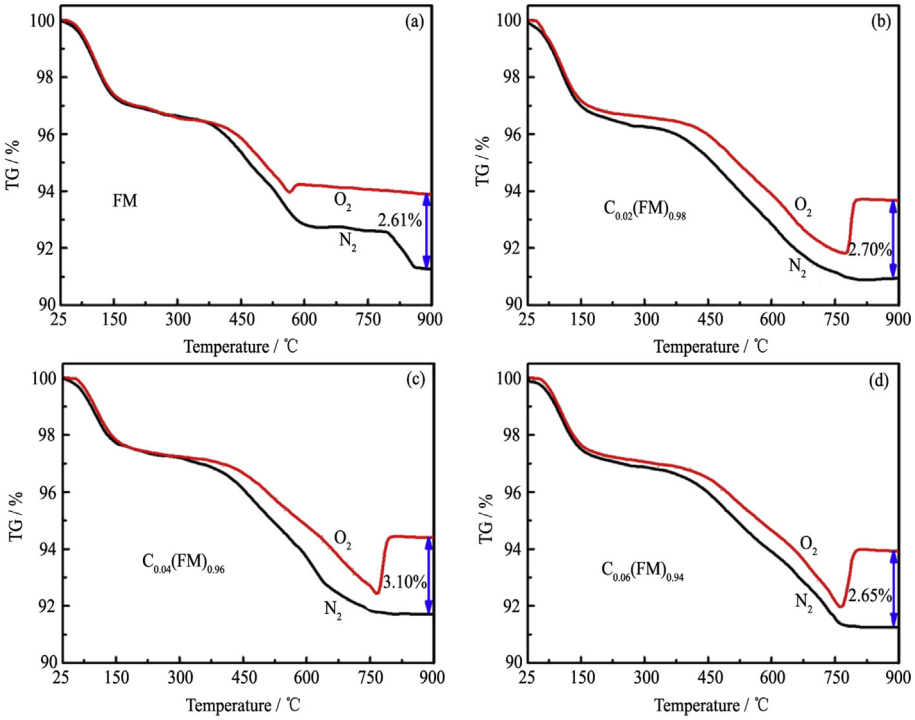

Fig. 4. TG curves of $C_x(FM)_{1-x}$ mixed oxide catalysts under flowing O_2 or N_2.

$C_x(FM)_{1-x}$ mixed oxides. In the FM sample, the reduction was separated into two sections. In the left section, three overlapped reduction peaks located at 204, 249 and 287 °C were attributed to the reduction of surface oxygen and MnO_x. In the right section, the two peaks at 409 and 637 °C were assigned to the reduction of Fe species.[21] The two new reduction peaks that occurred at 323 and 366 °C after Ce doping were attributed to the reduction of Ce species.[38] The reduction peaks of surface oxygen, MnO_x, and some Fe species moved to lower temperature because the addition of Ce introduced additional oxygen vacancies and enhanced the redox of the samples. Usually, the lower the starting reduction temperature is, the easier the reduce is.[39] However, the reduction peak located at above 500 °C moved to higher temperature because the addition of Ce led to some Fe_2O_3 precipitation. This also confirms the results of XRD and Raman characterization.

When the amount of oxygen vacancies is large on the surface of the sample, a weight increase is expected because the unsaturated surface is compensated by the oxygen when the sample is heated to a certain temperature under oxygen atmosphere.[40–43] Thus, the TG measurement can further provide the support for the oxygen vacancy. Fig. 4 shows the TG curves of $C_x(FM)_{1-x}$ mixed oxides heated to 900 °C under O_2 and N_2, respectively. The shapes of the TG curves of Ce-containing samples was obviously different from those of the FM sample, indicating that the introduction of a small amount of Ce greatly affects the physicochemical properties of FM mixed oxide, which was also confirmed in other characterizations. The weights of the $C_x(FM)_{1-x}$ mixed oxides were significantly increased when

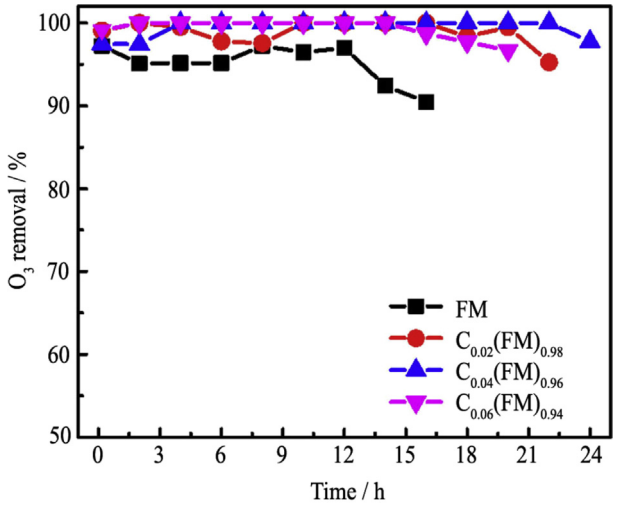

Fig. 5. Ozone catalytic decomposition on $C_x(FM)_{1-x}$ mixed oxide catalysts in dry gas. Reaction conditions: 21 ppm O_3, WHSV = 480000 mL/(g·h), 25 °C.

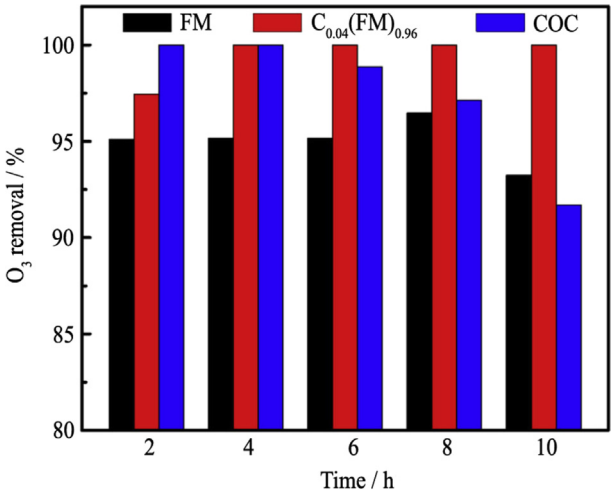

Fig. 6. Performance of different catalysts: FM, $C_{0.04}(FM)_{0.96}$, and commercial ozone catalyst (COC) for decomposing ozone in dry gas. Reaction conditions: 21 ppm O_3, WHSV = 480000 mL/(g·h), 25 °C.

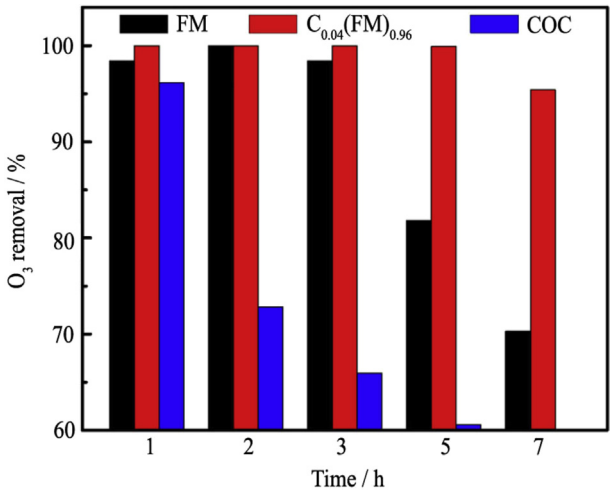

Fig. 7. Performance of different catalysts: FM, $C_{0.04}(FM)_{0.96}$, and commercial ozone catalyst (COC) for decomposing ozone in dry gas. Reaction conditions: 21 ppm O_3, WHSV = 480000 mL/(g·h), 0 °C.

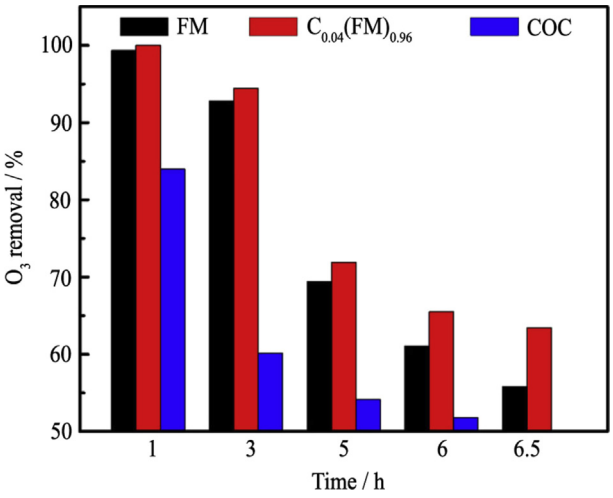

Fig. 8. Performance of different catalysts: FM, $C_{0.04}(FM)_{0.96}$, and commercial ozone catalyst (COC) for decomposing ozone in humid gas (65%). Reaction conditions: 21 ppm O_3, WHSV = 480000 mL/(g·h), 25 °C.

they were heated to a certain temperature under O_2. These increases further confirm the presence of abundant oxygen vacancies in these samples. The weight loss of the sample under N_2 can be ascribed to the removal of physical and chemical adsorbed

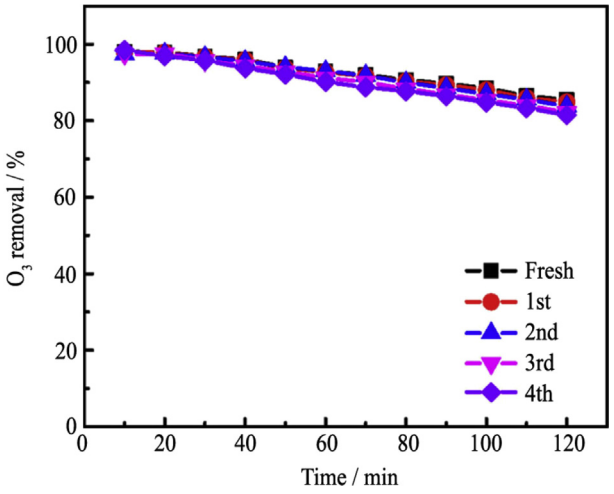

Fig. 10. Performance of $C_{0.04}(FM)_{0.96}$ mixed oxide catalysts after circulation and regeneration for decomposing ozone in dry gas. Reaction conditions: 130 ppm O_3, WHSV = 1200000 mL/(g·h), 25 °C.

substances, surface active oxygen and residues (such as citric acid) during preparation.[44] From the TG curves, these substances on the surface of the sample can be removed when the sample is heated to 900 °C under N_2. Therefore, based on TG data of $C_x(FM)_{1-x}$ mixed oxides under different atmosphere, we can roughly deduce the content of oxygen vacancies of these samples. The calculation results are shown in Fig. 4. A small amount of Ce doping can obtain more oxygen vacancies in the mixed oxides, and the $C_{0.04}(FM)_{0.96}$ sample has the most abundant oxygen vacancies.

3.3. Catalytic activity for ozone decomposition

The performance of as-synthesized $C_x(FM)_{1-x}$ mixed oxide catalysts for dry O_3 decomposition at 25 °C is presented in Fig. 5. Adding a small amount of Ce into FM mixed oxides can significantly improve the ability and stability of catalytic O_3 decomposition, and the $C_{0.04}(FM)_{0.96}$ mixed oxide exhibited the best activity, maintaining as high as 98% O_3 conversion after 24 h reaction; while for FM mixed oxide, the O_3 conversion decreased to 90% after 16 h reaction. This result indicates that doping of a small amount of Ce in FM mixed oxide is a simple and effective method for improving the catalytic performance of O_3 decomposition.

In order to further illustrate the performance advantages of as-synthesized Ce–Fe–Mn ternary mixed oxide catalysts, FM, $C_{0.04}(FM)_{0.96}$, and COC were selected for the catalytic performance test of O_3 decomposition under dry (0, 25 °C) and humid (25 °C) conditions, respectively. The results are shown in Figs. 6–8. The as-

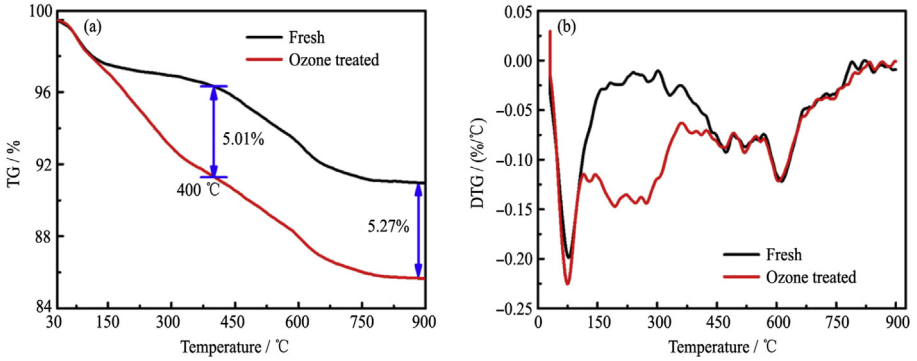

Fig. 9. TG (a) and DTG (b) curves of $C_{0.04}(FM)_{0.96}$ mixed oxide catalysts before and after treated with O_3 under flowing N_2.

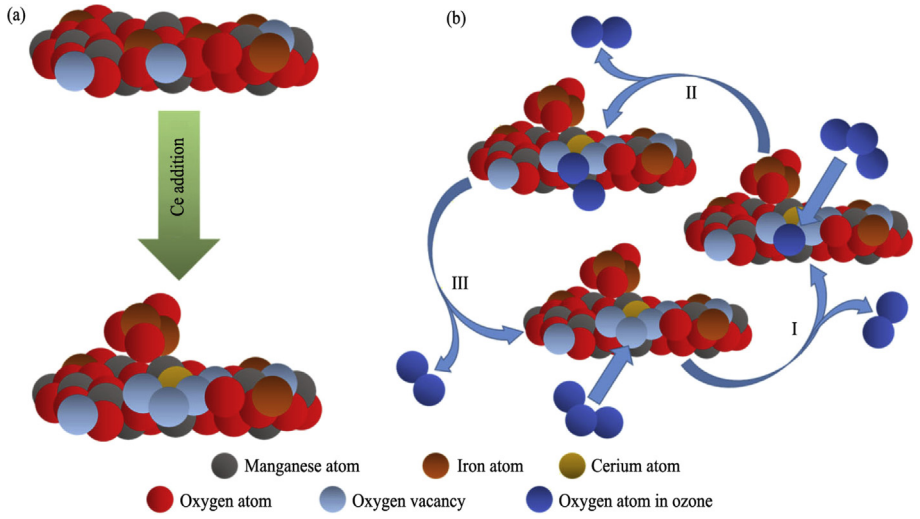

Fig. 11. Schematic representation of Ce effect on oxygen vacancies (a) and ozone catalytic decomposition on the $C_x(FM)_{1-x}$ mixed oxide catalysts (b).

synthesized $C_{0.04}(FM)_{0.96}$ mixed oxide catalyst exhibited better catalytic activity for O_3 decomposition under various experimental conditions. Especially under dry air (Figs. 6 and 7), $C_{0.04}(FM)_{0.96}$ has excellent activity and stability. As observed by many researchers,[21,45–47] water vapor has a negative impact on catalytic activity for O_3 decomposition (Fig. 8). This is because that the water molecules absorbed on the oxygen vacancies will dissociate to form hydroxyl groups, and more water molecules are connected to the hydroxyl groups by hydrogen bonds, which gradually cover the oxide surface.[48] But the data in Figs. 6–8 demonstrate that $C_{0.04}(FM)_{0.96}$ shows better activity not only in dry air but also in humid air than FM and COC. Therefore, Ce–Fe–Mn ternary mixed oxide catalyst is a promising O_3 decomposition catalyst.

3.4. Catalyst deactivation and regeneration

In addition to the above-mentioned decrease in catalytic O_3 activity caused by water vapor, it can be seen from Fig. 5 that the catalyst may also be deactivated during use. This may be because that the O_2^{2-} formed in the reaction cannot be decomposed in time, and the recovery of the occupied oxygen vacancies will be hindered, thus resulting in catalyst gradual deactivation.[21,23] TG analysis of the $C_{0.04}(FM)_{0.96}$ mixed oxide before and after O_3 treated (Fig. 9(a)) showed that the weight loss of the sample after O_3 treated increased significantly, and the weight loss mainly occurred before 400 °C, which is attributed to surface oxygen desorption.[21] TG measurement indirectly verified the cause of catalyst deactivation. Therefore, an effective catalyst regeneration method is to remove oxygen occupying oxygen vacancies. Combined with the DTG curves (Fig. 9(b)), we tried to regenerate the $C_{0.04}(FM)_{0.96}$ mixed oxide after O_3 treated in a muffle furnace at 200 °C for 2 h under air, and then test the activity (130 ppm O_3, 1200000 mL/(g·h), 25 °C) of the regenerated sample, the results are shown in Fig. 10. It is found that the activity of the $C_{0.04}(FM)_{0.96}$ mixed oxide could be restored by the heat treatment, and the activity was not significantly reduced after 4 cycles. So the deactivated Ce–Fe–Mn ternary mixed oxide catalyst can be reused by thermal regeneration.

3.5. Schematic of oxygen vacancy introduction and ozone decomposition

Fig. 11 shows the schematic of oxygen vacancy introduction and O_3 decomposition to deepen the understanding of the related processes. According to the characterization results of $C_x(FM)_{1-x}$ mixed oxides, the addition of a small amount of Ce into Mn–Fe mixed oxides causes lattice distortion, Fe separated out to form Fe_2O_3, and the defects increased, forming more oxygen vacancies, as shown in Fig. 11(a). In addition, many research findings show that oxygen vacancy is the active site for O_3 decomposition, and the content of oxygen vacancies is a decisive factor in catalytic O_3 decomposition.[20–24] According to the experimental results, the order of oxygen vacancies in the $C_x(FM)_{1-x}$ mixed oxide catalysts is $C_{0.04}(FM)_{0.96}$>$C_{0.02}(FM)_{0.98}$>$C_{0.06}(FM)_{0.94}$>FM and the order of catalytic O_3 decomposition is $C_{0.04}(FM)_{0.96}$>$C_{0.02}(FM)_{0.98}$>$C_{0.06}(FM)_{0.94}$>FM. This result is consistent with the reaction mechanism of oxygen vacancies as the active sites of catalytic O_3 decomposition. Therefore, the schematic of catalytic O_3 decomposition on $C_x(FM)_{1-x}$ mixed oxides is shown in Fig. 11(b), and the reported reaction equation is as follows[20]:

$$O_3 + O_{vac} \rightarrow O_2 + O^{2-} \quad (1)$$

$$O_3 + O^{2-} \rightarrow O_2 + O_2^{2-} \quad (2)$$

$$O_2^{2-} \rightarrow O_2 + O_{vac} \quad (3)$$

First, O_3 combines with oxygen vacancy (O_{vac}) on the surface of the catalyst. The oxygen vacancy transfers electrons to the oxygen atom to form O^{2-}, and an oxygen molecule is released (I). Then, another O_3 reacts with O^{2-} to form O_2^{2-}, while releasing an oxygen molecule (II). Finally, O_2^{2-} decomposes into an oxygen molecule, and the oxygen vacancy restored continues to participate in the next reaction (III). The reason of the catalyst deactivation is that O_2^{2-}cannot be decomposed in time for the restoration of oxygen vacancy and cannot participate in the reaction. Hence, introducing as many oxygen vacancies as possible is the most direct and effective means for promoting the catalytic O_3 decomposition of catalysts.

4. Conclusions

Ce–Fe–Mn ternary mixed oxide catalysts with enhanced activity and stability for O_3 decomposition than Mn–Fe binary mixed oxides have been obtained by introducing Ce during Mn–Fe mixed oxide synthesis. Based on the results of XRD, Raman and BET, defects are formed and the sizes of specific surface areas increase after the addition of Ce. These changes increase the number of reaction

sites. Furthermore, the FTIR, H_2-TPR, and TG results show that adding Ce increases the number of oxygen vacancies and thus greatly improves catalytic activity and stability for O_3 decomposition. The as-synthesized $C_{0.04}(FM)_{0.96}$ mixed oxide not only exhibits excellent catalytic performance of O_3 decomposition in dry gas but also shows more resistance to water vapor in humid gas. It also shows good catalytic performance in a low temperature environment (such as 0 °C). This finding indicates that introducing as many oxygen vacancies as possible is the most direct and effective means for developing efficient O_3 decomposition catalysts, and a ternary mixed oxide with a large number of oxygen vacancies is a good choice.

References

1. Mastsumi Y, Kawasaki M. Photolysis of atmospheric ozone in the ultraviolet region. *Chem Rev*. 2003;103(12):4767.
2. Yargeau V, Leclair C. Impact of operating conditions on decomposition of antibiotics during ozonation: a review. *Ozone Sci Eng*. 2008;30(3):175.
3. Rico D, Martin-Diana AB, Barat JM, Barry-Ryan C. Extending and measuring the quality of fresh-cut fruit and vegetables: a review. *Trends Food Sci Technol*. 2007;18(7):373.
4. Naydenov A, Konova P, Nikolov P, Klingstedt F, Kumar N, Kovacheva D, et al. Decomposition of ozone on Ag/SiO_2 catalyst for abatement of waste gases emissions. *Catal Today*. 2008;137(2–4):471.
5. Li Y, Hu C, Nie YL, Qu JH. Catalytic ozonation of selected pharmaceuticals over mesoporous alumina-supported manganese oxide. *Environ Sci Technol*. 2009;43(7):2525.
6. Dhandapani B, Oyama ST. Gas phase ozone decomposition catalysts. *Appl Catal B Environ*. 1997;11(2):129.
7. Heisig C, Zhang WM, Oyama ST. Decomposition of ozone using carbon-supported metal oxide catalysts. *Appl Catal B Environ*. 1997;14(1–2):117.
8. Yu QW, Pan H, Zhao M, Liu ZM, Wang JL, Chen YQ, et al. Influence of calcination temperature on the performance of $Pd–Mn/SiO_2–Al_2O_3$ catalysts for ozone decomposition. *J Hazard Mater*. 2009;172(2–3):631.
9. Oyama ST. Chemical and catalytic properties of ozone. *Catal Rev Sci Eng*. 2000;42(3):279.
10. Cooper OR, Parrish DD, Stohl A, Trainer M, Nédélec P, Thouret V, et al. Increasing springtime ozone mixing ratios in the free troposphere over western North America. *Nature*. 2010;463(7279):344.
11. Chen X, Zhao ZL, Zhou Y, Zhu QL, Pan ZY, Lu HF. A facile route for spraying preparation of Pt/TiO_2 monolithic catalysts toward VOCs combustion. *Appl Catal Gen*. 2018;566:190.
12. Destaillats H, Maddalena RL, Singer BC, Hodgson AT, McKone TE. Indoor pollutants emitted by office equipment: a review of reported data and information needs. *Atmos Environ*. 2008;42(7):1371.
13. Kumar N, Konova P, Naydenov A, Salmi T, Murzin DY, Heikillä T, et al. Ag-modified H-Beta, H-MCM-41 and SiO_2: influence of support, acidity and Ag content in ozone decomposition at ambient temperature. *Catal Today*. 2007;119(1–4):342.
14. Gall ET, Corsi RL, Siegel JA. Impact of physical properties on ozone removal by several porous materials. *Environ Sci Technol*. 2014;48(7):3682.
15. Darling E, Morrison GC, Corsi RL. Passive removal materials for indoor ozone control. *Build Sci*. 2016;106:33.
16. Spasova I, Nikolov P, Mehandjiev D. Ozone decomposition over alumina-supported copper, manganese and copper-manganese catalysts. *Ozone Sci Eng*. 2007;29(1):41.
17. Wang CX, Ma JZ, Liu FD, He H, Zhang RD. The effects of Mn^{2+} precursors on the structure and ozone decomposition activity of cryptomelane-type manganese oxide (OMS-2) catalysts. *J Phys Chem C*. 2015;119(40):23119.
18. Radhakrishnan R, Oyama ST. Electron transfer effects in ozone decomposition on supported manganese oxide. *J Phys Chem B*. 2001;105(19):4245.
19. Jiang CJ, Zhang PY, Zhang B, Li JG, Wang MX. Facile synthesis of activated carbon-supported porous manganese oxide via in situ reduction of permanganate for ozone decomposition. *Ozone Sci Eng*. 2013;35(4):308.
20. Jia JB, Zhang PY, Chen L. Catalytic decomposition of gaseous ozone over manganese dioxides with different crystal structures. *Appl Catal B Environ*. 2016;189:210.
21. Jia JB, Yang WJ, Zhang PY, Zhang JY. Facile synthesis of Fe-modified manganese oxide with high content of oxygen vacancies for efficient airborne ozone destruction. *Appl Catal Gen*. 2017;546:79.
22. Lian ZH, Ma JZ, He H. Decomposition of high-level ozone under high humidity over Mn–Fe catalyst: the influence of iron precursors. *Catal Comun*. 2015;59:156.
23. Liu Y, Zhang PY. Catalytic decomposition of gaseous ozone over todorokite-type manganese dioxides at room temperature: effects of cerium modification. *Appl Catal Gen*. 2017;530:102.
24. Zhu GX, Zhu JG, Jiang WJ, Zhang ZJ, Wang J, Zhu YF, et al. Surface oxygen vacancy induced α-MnO_2 nanofiber for highly efficient ozone elimination. *Appl Catal B Environ*. 2017;209:729.
25. Dhar GM, Srinivas BN, Rana MS, Kumar M, Maity SK. Mixed oxide supported hydrodesulfurization catalysts—a review. *Catal Today*. 2003;86(1–4):45.
26. Zhang LJ, Meng M, Wang XJ, Zhou S, Yang LJ, Zhang TY, et al. A series of copper-free ternary oxide catalysts $ZnAlCe_x$ used for hydrogen production via dimethyl ether steam reforming. *J Power Sources*. 2014;268:331.
27. Choi KH, Lee DH, Kim HS, Yoon YC, Park CS, Kim YH. Reaction characteristics of precious-metal-free ternary Mn-Cu-M (M = Ce, Co, Cr, and Fe) oxide catalysts for low-temperature CO oxidation. *Ind Eng Chem Res*. 2016;55(16):4443.
28. Lu HF, Kong XX, Huang HF, Zhou Y, Chen YF. Cu–Mn–Ce ternary mixed oxide catalysts for catalytic combustion of toluene. *J Environ Sci*. 2015;32:102.
29. Rodriguez-Talavera R, Vargas S, Arroyo-Murillo R, Montiel-Campos R, Haro-Poniatowski E. Modification of the phase transition temperatures in titania doped with various cations. *J Mater Res*. 1997;12(2):439.
30. Shah HU, Wang FP, Javed MS, Ahmad MA, Saleem M, Zhan JB, et al. In-situ growth of MnO_2 nanorods forest on carbon textile as efficient electrode material for supercapacitors. *J Energy Storage*. 2018;17:318.
31. Bekana D, Liu R, Li SS, Lai YJ, Liu JF. Facile fabrication of silver nanoparticle decorated a-Fe_2O_3 nanoflakes as ultrasensitive surface-enhanced Raman spectroscopy substrates. *Anal Chim Acta*. 2018;1006:74.
32. Lu HF, Zhang PF, Qiao ZA, Zhang JS, Zhu HY, Chen JH, et al. Ionic liquid-mediated synthesis of meso-scale porous lanthanum-transition-metal perovskites with high CO oxidation performance. *Chem Commun*. 2015;51(27):5910.
33. Li LL, Chu Y, Liu Y, Dong LH. Synthesis and shape evolution of novel cuniform-like MnO_2 in aqueous solution. *Mater Lett*. 2007;61(7):1609.
34. Zhao B, Wang YC, Guo H, Wang J, He YD, Jiao Z, et al. Iron oxide(III) nanoparticles fabricated by electron beam irradiation method. *Mater Sci*. 2007;25(4):1609.
35. Zhang WW, Chen DH. Preparation and performance of CeO_2 hollow spheres and nanoparticles. *J Rare Earths*. 2016;34(3):295.
36. Gong SY, Chen JY, Wu XF, Han N, Chen YF. *In-situ* synthesis of Cu_2O/reduced graphene oxide composite as effective catalyst for ozone decomposition. *Catal Comun*. 2018;106:25.
37. Yang SC, Su WN, Rick J, Lin SD, Liu JY, Pan CJ, et al. Oxygen vacancy engineering of cerium oxides for carbon dioxide capture and reduction. *ChemSusChem*. 2013;6(8):1326.
38. Wu XD, Yu HN, Weng D, Liu S, Fan J. Synergistic effect between MnO and CeO_2 in the physical mixture: electronic interaction and NO oxidation activity. *J Rare Earths*. 2013;31(12):1141.
39. Liu XW, Zhou KB, Wang L, Wang BY, Li YD. Oxygen vacancy clusters promoting reducibility and activity of ceria nanorods. *J Am Chem Soc*. 2009;131(9):3140.
40. Liu BM, Zhang GZ, Zhang K, Kuroiwa Y, Moriyoshi Y, Yu HM, et al. Unconventional luminescent centers in metastable phases created by topochemical reduction reactions. *Angew Chem Int Ed*. 2016;55(16):4967.
41. Li JL, Zhang M, Guan ZJ, Li QY, He CQ, Yang JJ. Synergistic effect of surface and bulk single-electron-trapped oxygen vacancy of TiO_2 in the photocatalytic reduction of CO_2. *Appl Catal B Environ*. 2017;206:300.
42. Li LC, Shi KZ, Tu R, Qian Q, Li D, Yang ZH, et al. Black TiO_2(B)/anatase bicrystalline TiO_{2-x} nanofibers with enhanced photocatalytic performance. *Chin J Catal*. 2015;36(11):1943.
43. Sun CC, He GZ, Gao LC, Song SL, Li R, Zhen Q. Absorption behavior of lattice oxygen in $Ce_{0.8}Y_{0.2}O_{2-\delta}$ at intermediate temperature. *J Rare Earths*. 2018;36(6):630.
44. Zhu GX, Zhu JG, Li WL, Yao WQ, Zong RL, Zhu YF, et al. Tuning the K^+concentration in the tunnels of α-MnO_2 to increase the content of oxygen vacancy for ozone elimination. *Environ Sci Technol*. 2018;52:8684.
45. Einaga H, Harada M, Futamura S. Structural changes in alumina-supported manganese oxides during ozone decomposition. *Chem Phys Lett*. 2005;408:377.
46. Liu CA, Sun DZ, Wang H, Li W. Catalysts for decomposing ozone tail gas. *J Environ Sci*. 2003;15:779.
47. Huang HB, Ye XG, Huang WJ, Chen JD, Xu Y, Wu MY, et al. Ozone-catalytic oxidation of gaseous benzene over MnO_2/ZSM-5 at ambient temperature: catalytic deactivation and its suppression. *Chem Eng J*. 2015;264:24.
48. Chen BH, Ma YS, Ding LB, Xu LS, Wu ZF, Yuan Q, et al. Reactivity of hydroxyls and water on a CeO_2(111) thin film surface: the role of oxygen vacancy. *J Phys Chem C*. 2013;117:5800.